Joule

Article

Stabilizing lithium plating in polymer electrolytes by concentration-polarization-induced phase transformation

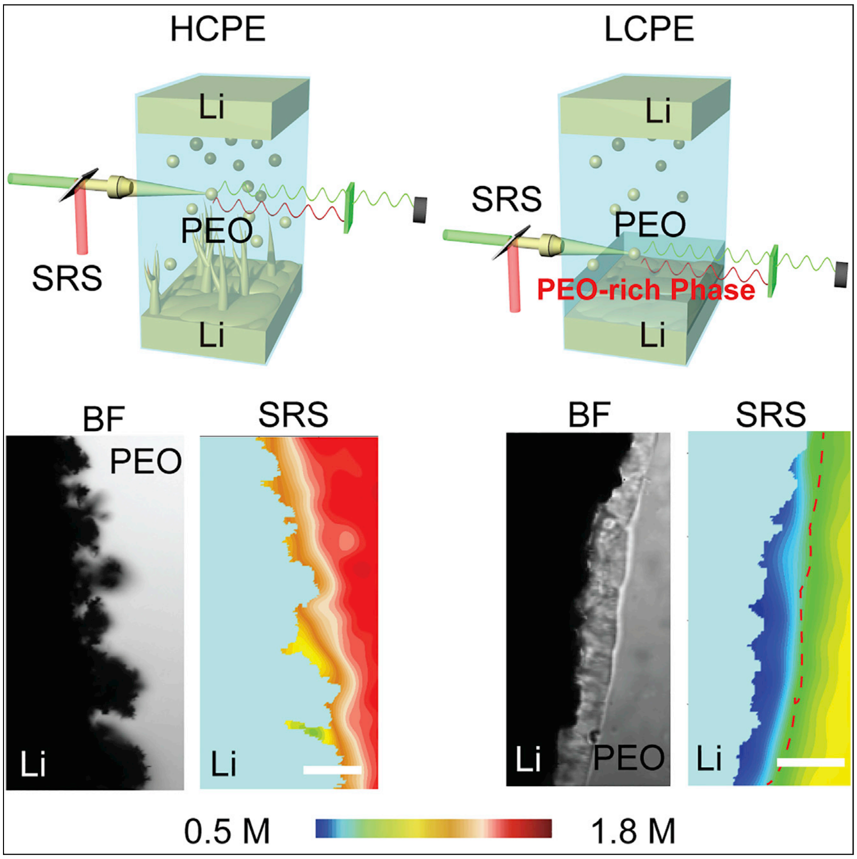

Stimulated Raman scattering microscopy is used to study complicated ion transport and phase-evolution processes in polymer electrolytes and shows that a new phase can be formed on lithium metal surfaces during polarization. The new phase is mechanically rigid to suppress lithium whisker growth. Based on this discovery, we propose a phase-diagram-driven design protocol for poly(ethylene oxide) electrolytes so that the charging current can induce the formation of a mechanically rigid phase on the lithium metal surface to achieve a stable lithium plating.

Qian Cheng, Tianwei Jin, Yupeng Miao, ..., Ju Li, Wei Min, Yuan Yang

qc2227@columbia.edu (Q.C.)
wm2256@columbia.edu (W.M.)
yy2664@columbia.edu (Y.Y.)

Highlights

- Stimulated Raman scattering microscopy reveals phase evolution in a polymer electrolyte
- The formation of a stiff PEO-rich phase can suppress lithium whisker growth
- A phase-diagram-driven design protocol for stable lithium plating is developed

Cheng et al., Joule 6, 1–18
October 19, 2022 © 2022 Elsevier Inc.
https://doi.org/10.1016/j.joule.2022.08.001

Please cite this article in press as: Cheng et al., Stabilizing lithium plating in polymer electrolytes by concentration-polarization-induced phase transformation, Joule (2022), https://doi.org/10.1016/j.joule.2022.08.001

Joule CellPress

Article

Stabilizing lithium plating in polymer electrolytes by concentration-polarization-induced phase transformation

Qian Cheng,[1,8,*] Tianwei Jin,[1,8] Yupeng Miao,[2,8] Zhe Liu,[3] James Borovilas,[1] Hanrui Zhang,[1] Shuwei Liu,[1] So-Yeon Kim,[4] Ruiwen Zhang,[1] Haozhen Wang,[5] Xi Chen,[5,6] Long-Qing Chen,[3] Ju Li,[4,7] Wei Min,[2,*] and Yuan Yang[1,9,*]

SUMMARY

It is widely accepted that concentration polarization in liquid electrolytes promotes whisker growth during metal deposition, and therefore, high salt concentration is favored. Here, we report unexpected opposite behaviors in solid polymer electrolytes: concentration polarization can induce phase transformation in a polyethylene oxide (PEO) electrolyte, forming a new PEO-rich but salt-/plasticizer-poor phase at the lithium/electrolyte interface, as unveiled by stimulated Raman scattering microscopy. The new phase has a significantly higher Young's modulus (~1–3 GPa) than a bulk polymer electrolyte (<1 MPa). We hereby propose a design rule for PEO electrolytes: their compositions should be near the boundary between single-phase and two-phase regions in the phase diagram so that the applied current can induce the formation of a mechanically rigid PEO-rich phase to suppress lithium whiskers. $LiFePO_4$/PEO/Li cells with concentration-polarization-induced phase transformation can be reversibly cycled 100 times, while cells without such transformation fail within 10 cycles, demonstrating the effectiveness of this strategy.

INTRODUCTION

Lithium metal batteries (LMBs) have attracted significant attention in recent years as next-generation batteries with a high energy density.[1–3] An Li metal anode has a theoretical capacity of 3,860 mAh g^{-1}, ten times that of a conventional graphite anode, and an ultralow electrode potential (–3.04 V versus a standard hydrogen electrode). However, lithium deposition is prone to being non-uniform, leading to rough morphologies such as mossy and dendritic lithium.[4–7] Such uneven deposition not only results in a large electrode surface area, which promotes side reactions with electrolytes and decreases Coulombic efficiency (CE) and cycle life,[8,9] but also imposes potential safety hazards such as internal shorting and thermal runaway, especially in combination with conventional flammable liquid electrolytes (e.g., ethers and carbonates).[10–13]

Although polymer electrolytes cannot fully resolve the safety issues in LMBs, they can help to enhance the thermal stability of LMBs as they are more thermally stable than liquid electrolytes.[14–16] For example, the flash point (f.p.) of poly (ethylene oxide) (Mw ~ 600,000) is 250°C,[17] much higher than dimethyl carbonate (21.5°C),[18] 1,3-dioxolane (2°C),[19] and 1,2-dimethoxyethane (−2°C).[17] Polymer electrolytes

CONTEXT & SCALE

Polymer electrolytes are drawing increasing interest in terms of their use in batteries because of their high thermal stability and chemical compatibility with lithium metal, but they are usually soft and unable to suppress Li whisker growth, resulting in poor cycling and safety concerns. The salt-concentration-dependent transport and phase dynamics in the electrolyte were often omitted in past studies. In this work, by using an emerging stimulated Raman microscopy, we unveiled a polarization-induced phase-separation process on the anode surface, which forms a mechanically rigid PEO-rich phase with a high Young's modulus (~1–3 GPa) at the electrolyte/lithium interface and suppresses lithium whisker growth. We further propose a phase-diagram-driven design protocol to realize uniform lithium deposition in polymer electrolytes. This work highlights the significance of phase dynamics in polymer electrolytes and holds the potential to help with better understanding and improving the performance of electrochemical devices with polymer electrolytes.

Please cite this article in press as: Cheng et al., Stabilizing lithium plating in polymer electrolytes by concentration-polarization-induced phase transformation, Joule (2022), https://doi.org/10.1016/j.joule.2022.08.001

are also compatible with conventional battery manufacturing processes and are easy to scale up.[20] Unfortunately, Young's moduli of polyethylene oxide (PEO) electrolytes, typically in the range of 20–70 MPa,[21–23] are much lower than the proposed threshold of 1 GPa needed to effectively suppress Li whiskers.[11,24] Hence, the fast growth of Li whiskers in polymer electrolytes is widely observed in literature[24–26] and can be seen in Video S1. The whisker growth becomes even more severe with the introduction of plasticizers for enhancing ionic conductivity, as they further soften polymer electrolytes.[23,27] This issue is difficult to fully resolve by ceramic additives,[28] as lithium whiskers can still penetrate through interspace between ceramic fillers. Currently, lithium whisker growth remains one of the major challenges in polymer-electrolyte-based LMBs.[29]

Addressing this challenge requires a fundamental understanding of the embedded dynamic Li metal/polymer electrolyte interface, such as how Li^+ heterogeneity evolves at the Li anode surface and how the Li anode interacts with solid electrolytes. Although remarkable advances have been achieved recently in characterizing Li anodes and the solid electrolyte interphase (SEI), such as cryo-transmission electron microscopy (TEM),[30–32] nuclear magnetic resonance (NMR),[33,34] *in situ* and environmental TEM,[35,36] synchrotron,[37,38] and ambient pressure X-ray photoelectron spectroscopy (XPS),[39] there is limited progress toward imaging the interaction between Li^+ ion transport in the electrolyte and Li whisker growth. This arises from challenges in visualizing ions in electrolytes, which not only have a low concentration (0–2 M) but also possess fast dynamics (diffusivity of $\sim 10^{-7}$–10^{-6} cm^2 s^{-1}) compared with solid electrode materials (10–50 M, and $<10^{-9}$ cm^2 s^{-1}). Hence, ultrahigh chemical sensitivity (~1–10 mM), high speed (~1 s/image), and fine spatial resolution (<1 μm) are simultaneously required to image chemical dynamics in electrolytes, such as salt concentration polarization. Such resolution and sensitivity are beyond the capability of conventional characterization tools. Recently, Steinrück et al. obtained both a 1D concentration profile and salt velocity using X-ray photon correlation spectroscopy (XPCS) and X-ray absorption microscopy (XAM). This represents an important step in imaging and understanding ion transport in polymer electrolytes.[40]

We previously utilized stimulated Raman scattering (SRS) microscopy to image the ion transport profile in liquid electrolytes, which simultaneously offers high sensitivity (< 1 mM), fast imaging speed (~2 μs per pixel), and fine spatial resolution (down to 300 nm).[41–43] SRS microscopy uses two temporally and spatially synchronized laser beams with an energy difference equal to that of the targeted bond's vibrational mode (Note S1). The synergy of the two beams amplifies the otherwise weak vibrational signal by up to 10^8 times and thus enables the desired temporal resolution, imaging speed, and sensitivity (Figures 1A and S1).[44] SRS is becoming an emerging technique for materials science.[41,45] Using this emerging microscopy, we visualized for the first time the heterogeneity of ion depletion in liquid electrolytes due to concentration polarization and how it correlated with lithium dendrite growth.[41] We observed that ion depletion at the Li/electrolyte interface led to faster whisker growth due to an enhanced electrical field and larger concentration heterogeneity, which agreed with the theoretical predictions.[1,46]

In this report, we further explored solid polymer electrolyte (SPE)/electrode interaction and observed unexpected opposite phenomena. Instead of promoting whiskers, concentration polarization reduces salt concentration at the lithium/electrolyte interface and transforms the single-phase PEO electrolyte into the two-phase one. This induces the formation of a mechanically rigid PEO-rich phase with a modulus

[1]Program in Materials Science and Engineering, Department of Applied Physics and Applied Mathematics, Columbia University, New York, NY 10027, USA

[2]Department of Chemistry, Columbia University, New York, NY 10027, USA

[3]Department of Materials Science and Engineering, The Pennsylvania State University, University Park, State College, PA 16802, USA

[4]Department of Materials Science and Engineering, Massachusetts Institute of Technology, Cambridge, MA 02139, USA

[5]Advanced Science Research Center (ASRC), City University of New York, 85 St. Nicholas Terrace, New York, NY 10031, USA

[6]Department of Chemical Engineering, The City College of New York, 160 Convent Avenue, New York, NY 10031, USA

[7]Department of Nuclear Science and Engineering, Massachusetts Institute of Technology, Cambridge, MA 02139, USA

[8]These authors contributed equally

[9]Lead contact

*Correspondence: qc2227@columbia.edu (Q.C.), wm2256@columbia.edu (W.M.), yy2664@columbia.edu (Y.Y.)

https://doi.org/10.1016/j.joule.2022.08.001

Please cite this article in press as: Cheng et al., Stabilizing lithium plating in polymer electrolytes by concentration-polarization-induced phase transformation, Joule (2022), https://doi.org/10.1016/j.joule.2022.08.001

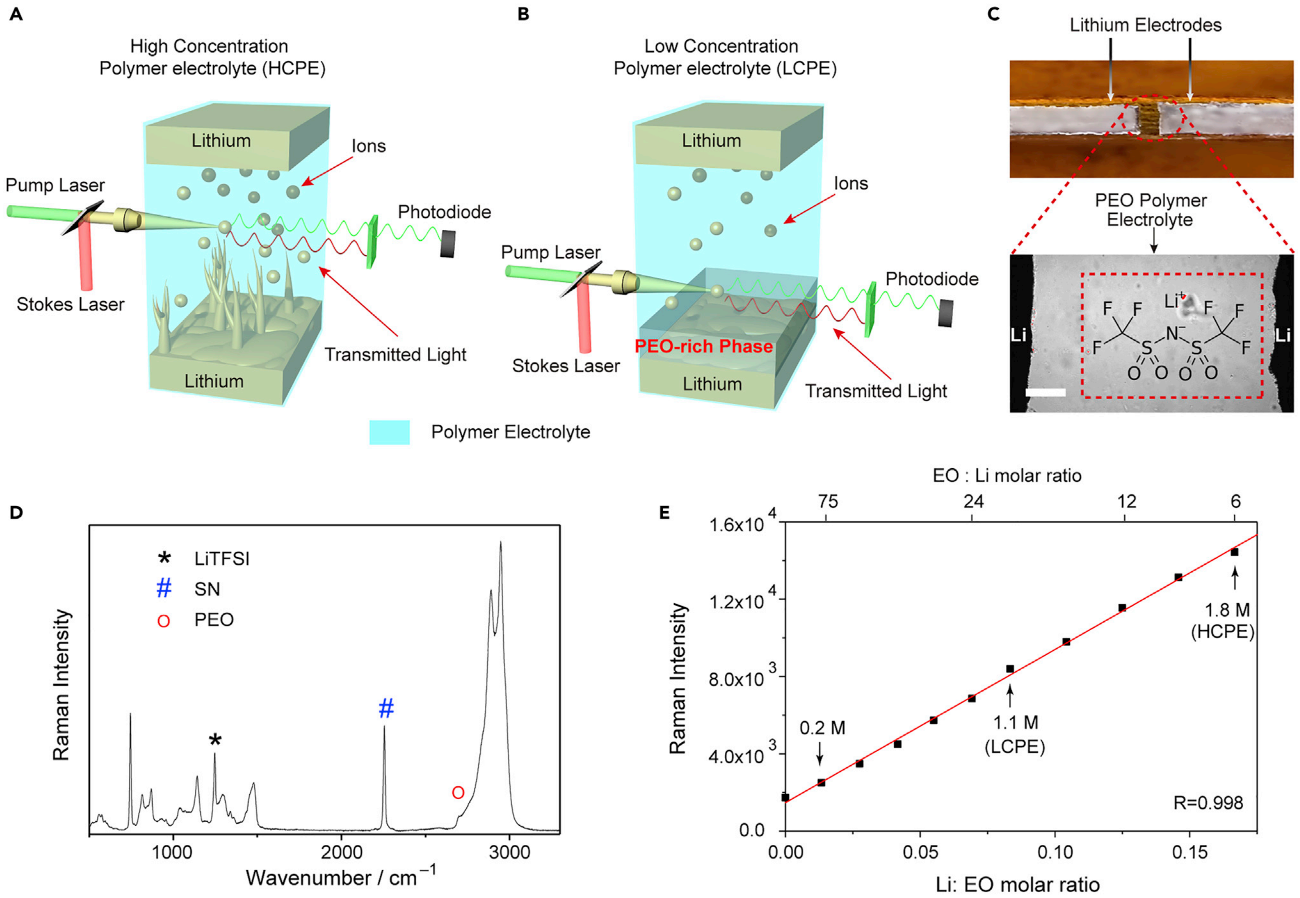

Figure 1. The schematics of *operando* SRS imaging of the Li/PEO electrolyte interface

(A and B) The schematics of SRS imaging of (A) a high-concentration polymer electrolyte (HCPE) and (B) a low-concentration polymer electrolyte (LCPE) in Li/Li cells. In LCPE, the polarization-induced phase transformation leads to a mechanically strong PEO-rich phase at the lithium/electrolyte interface, which helps suppress lithium whiskers.

(C) The bright-field image of a Li/PEO/Li cell. The upper picture shows the architecture of the cell, and the lower one shows a zoom-in image taken by an optical microscope. Scale bar is 100 μm.

(D) The Raman spectrum of LCPE, where fingerprint peaks for LiTFSI, SN, and PEO are labeled. The corresponding composition of LCPE is EO:Li:SN = 12:1:2.64 (molarity).

(E) The plot of Raman intensity of the LiTFSI peak at 1,245 cm^{-1} versus the Li:EO ratio in PEO electrolytes with 40 wt % SN, showing good linearity. The points of 1.1 and 1.8 M LiTFSI correspond to LCPE and HCPE, respectively.

of ~1–3 GPa at the lithium/electrolyte interface, corresponding to a shear modulus of 0.36–1.06 GPa (Figure 1B). Such a high modulus suppressed whisker growth and led to uniform lithium deposition. Based on this discovery, we propose a design rule of polymer electrolytes for lithium metal anodes: electrolyte composition should be at the boundary between the single-phase and two-phase regions in the PEO-salt-plasticizer phase diagram so that a slight salt concentration polarization induced by a small current can form the mechanically rigid PEO-rich phase on the lithium metal surface to passivate lithium metal. This design rule guides us to further develop a PEO electrolyte with an optimal composition (ethylene oxide [EO]; EO:Li = 12:1 with 40 wt % plasticizer, 1.1 M Li salt), which showed stable cycling over 100 times in an $LiFePO_4$ (LFP)/PEO/Li cell at 40°C. In contrast, LFP/PEO/Li cells with concentrated PEO electrolytes (EO/Li = 6:1 with 40 wt % plasticizer, 1.8 M Li salt) failed quickly after 10 cycles due to the rapid growth of lithium whiskers and dramatically increased impedance.

Please cite this article in press as: Cheng et al., Stabilizing lithium plating in polymer electrolytes by concentration-polarization-induced phase transformation, Joule (2022), https://doi.org/10.1016/j.joule.2022.08.001

RESULTS

SRS imaging of Li/SPE interaction

Home-made parallel cells were used to visualize Li/PEO electrolyte interaction via SRS microscopy (Figure 1C). In this cell, the PEO electrolyte filled in the gap between two pieces of lithium, and all components were sandwiched between two glass slides and sealed by epoxy. The distance between the two electrodes was typically around 0.5 mm. The PEO electrolyte contained lithium bis (trifluoromethane sulfonyl) imide (LiTFSI) as the salt and succinonitrile (SN) as the plasticizer[47] to enhance ionic conductivity and enable operation at room temperature (RT). Although SN is not stable with lithium metal in the long term, it generally only affects the cycling performance after 100 cycles. Details of electrolyte composition and fabrication processes can be found in experimental procedures. Wavenumbers at 1,245 cm^{-1} (C–F stretching),[48] 2,250 cm^{-1} ($C\equiv N$ stretching),[49] and 2,800 cm^{-1} (C–H stretching with combination vibration)[50] were selected as Raman signatures of LiTFSI, SN, and PEO, respectively (Figure 1D). Due to the requirement of electroneutrality, $[Li^+]$ could be considered to be equal to $[TFSI^-]$, even at the nanoscale (Note S2), with an error smaller than 0.1 mM.[41] Therefore, $[TFSI^-]$ was measured to represent the local $[Li^+]$. The Raman intensities of $TFSI^-$ were proportional to its concentration, and hence the Raman signal could be easily converted to chemical concentration (Figure 1E). It is worth noting that LiTFSI in the PEO-rich phase may have different Raman cross sections, which may introduce small errors into the calibration curve in Figure 1E (Figure S2; Note S3).[51] The chemical sensitivity of LiTFSI was calculated to be 0.012 M.

Lithium growth in PEO electrolytes with different salt concentrations

As two representatives, the high-concentration polymer electrolyte (HCPE) and the low-concentration polymer electrolyte (LCPE) were studied with EO:Li:SN = 12:2:2.64 and 12:1:2.64 in molarity, respectively, which correspond to 1.8 M LiTFSI and 2.4 M SN for HCPE, and 1.1 M LiTFSI and 2.9 M SN for LCPE, respectively. The weight ratios of SN to PEO were fixed at 40% in both cases. Cyclic voltammetry showed that both electrolytes have no appreciable side reaction between 0 and 4 V versus Li^+/Li and were capable of reversible lithium plating and stripping (Figure S3). The portion of ion pairs/aggregates is relatively small (~10%–20%, Table S1; Figure S4), so its effect is not considered in our analysis (see Note S4 for details), and the ionic conductivities of HCPE and LCPE are 1.7×10^{-4} S cm^{-1} and 1.0×10^{-4} S cm^{-1} at RT, respectively (Figure S5). Due to the relatively low ionic conductivities at RT, a current density of 0.5 mA cm^{-2} was applied.

In the case of HCPE (Figure 2A; Video S2), the applied current gradually consumed $[Li^+]$ on the lithium surface ($[Li^+]_{0\ \mu m}$) from 1.8 M at t = 0 to 1.2 M at t = 27 min, after which $[Li^+]_{0\ \mu m}$ remained stable at ~1.2 M in a steady state (Figures 2B and 2C). Meanwhile, the lithium growth rate (v) quickly increased from 0.27 ± 0.18 μm min^{-1} at t = 0 to 0.9 ± 0.46 μm min^{-1} at t = 27 min (Figure 2D). The growth was in the form of mossy lithium, and statistical analysis showed a normal distribution of v (Figures S6A–S6C). Afterward, v was drastically increased to ~1.5 μm min^{-1} for the remaining time, leading to an ultrahigh porosity of 97%, indicating that the HCPE could not suppress whisker growth. At this stage, a dual-peak normal distribution of v was observed (Figures S6D–S6H), where v was low in part of the surface (< 1 μm min^{-1}) but ultrahigh in other regions (> 2 μm min^{-1}), showing the heterogeneous whisker growth on the lithium electrode. This dual-peak mode may arise from SEI properties and non-uniform concentration polarization of ions. These results show that if no phase transformation occurs, ion concentration

Please cite this article in press as: Cheng et al., Stabilizing lithium plating in polymer electrolytes by concentration-polarization-induced phase transformation, Joule (2022), https://doi.org/10.1016/j.joule.2022.08.001

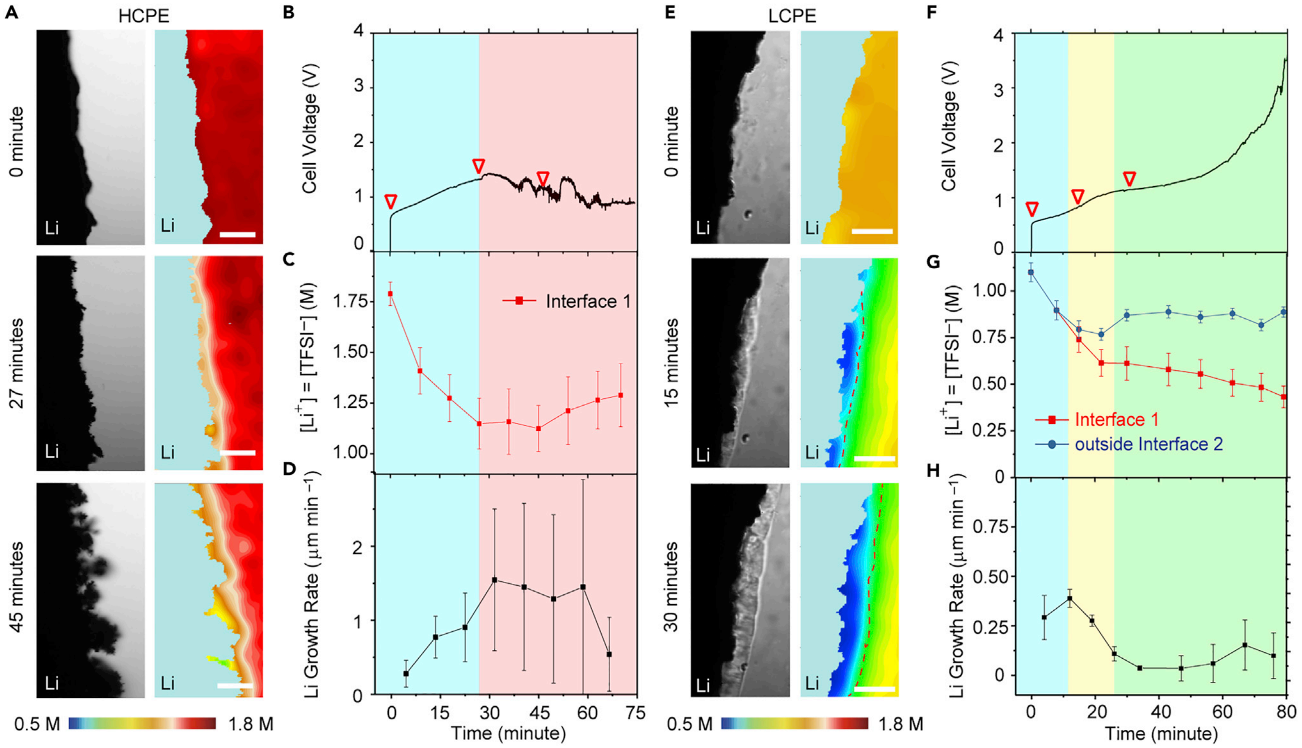

Figure 2. Lithium growth at the lithium/PEO electrolyte interface with HCPE or LCPE

(A–D) Lithium whisker growth in HCPE. (A) The bright-field and corresponding SRS images of $[Li^+] = [TFSI^-]$ at three representative stages. (B) The voltage profile of the Li/Li cell in (A). (C) $[Li^+] = [TFSI^-]$ versus time, and (D) the lithium growth rate (*v*) versus time. Interface 1 refers to the boundary between the lithium electrode and the PEO electrolyte.

(E–H) Lithium growth in LCPE. (E) The bright-field and SRS images of $[Li^+]$ at three representative moments. (F) The voltage profile of the Li/Li cell in (E). The yellow shading corresponds to the appearance of the PEO-rich phase, and the green shading indicates the region where the PEO-rich phase has covered the entire lithium surface. (G) $[Li^+] = [TFSI^-]$ versus time, and (H) the lithium growth rate (*v*) versus time. Interface 2 refers to the boundary between the new PEO-rich phase and the isotropic bulk polymer electrolyte, as marked by dash lines in SRS images in (E). Scale bars are 50 μm. Error bars represent standard deviation. Zoom-in SRS images of (A) and (E) are shown in Figure S8. The electrode distances are 500 μm for both cells. Both cells were applied with a current density of 0.5 mA cm^{-2} at room temperature.

polarization at the Li/polymer electrolyte interface promotes whisker growth (Video S2), similar to our previous observations in a gel electrolyte.[41]

In contrast to the conventional behaviors observed in HCPE, we find that concentration polarization in LCPE induced a phase transformation process at the lithium/electrolyte interface that unexpectedly suppressed lithium whisker growth, as observed by both SRS and bright-field (BF) images (Figures 2E and 2F; Video S2). First, the new phase appeared as the blue region in SRS and the granular-like region in BF, which was also confirmed by the Raman spectra (Figure S7). The spontaneous Raman spectra of the PEO-rich phase matched with those of PEO spherulites, suggesting its semi-crystalline nature. This new phase only contained PEO, SN, and LiTFSI, and no obvious peaks of decomposition products such as Li_2O and RO-Li were detected. The PEO-rich phase had a much lower [LiTFSI] than that in the adjacent isotropic bulk LCPE, as shown by the contrast between [LiTFSI] at the Li/electrolyte interface (interface 1), and [LiTFSI] outside the boundary between the new phase and the isotropic bulk electrolyte (interface 2) (Figure 2G). This difference increased from 0.79 versus 0.74 M at t = 15 min, to 0.87 versus 0.61 M at t = 30 min, and 0.89 versus 0.43 M at t = 79 min. Further study showed that the new phase was also poor in SN, and [SN] was only ~1.8 M at the interface compared with 3.8 M outside interface 2 (Figures S9 and S10).

Please cite this article in press as: Cheng et al., Stabilizing lithium plating in polymer electrolytes by concentration-polarization-induced phase transformation, Joule (2022), https://doi.org/10.1016/j.joule.2022.08.001

Although the PEO-rich phase is poor in LiTFSI and SN, their concentrations are well above 0 M throughout the whole lithium deposition process. Therefore, the PEO-rich layer still has a moderate ionic conductivity of ~2–5 × 10^{-5} S cm^{-1} (Figure S11). In addition, the limiting current density and Sand's time of this cell are 0.28 mA cm^{-2} and 162 min, respectively (Note S5; Figure S12), so the large voltage polarization observed at t = 79 min is more likely caused by the increasing thickness of the PEO-rich phase instead of complete ion depletion. Given that the deposition time is less than the Sand's time and the concentration is well above 0 M, the observed non-uniform deposition in this work should be considered as whiskers or mossy lithium.[46]

The appearance of this new phase unexpectedly—but effectively—suppressed the growth of lithium whiskers. Although the lithium whisker growth was observed at t = 0 with *v* of ~0.3 μm min^{-1} (87% porosity), *v* quickly dropped to 0.048 μm/min at t = 30 min after the initial formation of the PEO-rich phase (Figure 2H), equivalent to a porosity of 16%. At this stage, the PEO-rich phase progressively formed on the lithium metal surface. After the new phase fully covered the Li metal surface, the average *v* from 30 to 63 min was only 0.044 μm min^{-1}, which corresponded to a low porosity of 9.2%, about one-thirtieth of that in HCPE, indicating a dense and uniform lithium deposition. Such behavior is not only self-forming but also self-reinforcing during concentration polarization. For example, if a lithium whisker grows fast at a certain location, the local current density will increase and lead to larger concentration polarization and hence the formation of a thicker PEO-rich phase, which in turn suppresses whisker growth (Video S1, LCPE). This active protection mechanism is distinct from other conventional passive protective layers, which require perfect uniformity and durability. This suppression mechanism has not been reported in literature, to the best of the authors' knowledge.

The relation between electrolyte composition and formation of the PEO-rich phase

To understand how phase transformation in LCPE occurs, we characterized its evolution using spontaneous Raman scattering spectroscopy (Figure S13). During the formation of this PEO-rich phase, we observed rising peaks at 832, 1,268, and 1,467 cm^{-1}, which correspond to semi-crystalline PEO.[52] Meanwhile, peaks for $TFSI^-$ (730, 802, and 1,245 cm^{-1}) decreased simultaneously and salt concentrations derived from different peaks were nearly identical (Figure S14). After the applied current was reversed, the PEO-rich layer gradually diminished, as observed in BF images. Meanwhile, the intensity of LiTFSI peaks gradually recovered and that of semi-crystalline PEO peaks slowly decreased, showing that the formation of this layer was reversible (Figure S13C). Therefore, this layer was determined to be a PEO-rich and salt-poor phase but without any decomposition products of the electrolyte. We also examined the composition of SEI on lithium metal for both LCPE and HCPE, which have similar compositions (Figure S15; Tables S2 and S3). This indicates that the difference in SEI is not responsible for the distinct lithium deposition behaviors we observed.

After excluding the possibility of electrolyte decomposition, we constructed the ternary phase diagram of PEO-LiTFSI-SN to understand composition-dependent phase evolution. This was achieved with the assistance of SRS (Figure 3A), as it measured the composition of each phase in a high-throughput fashion. The phase diagram illustrates a single-phase isotropic zone (I-zone) in the middle (orange) and three two-phase regions at the corners (white and contour region). Representative SRS images of each region are shown in Figure S16. As shown in Figure 3A, the

Please cite this article in press as: Cheng et al., Stabilizing lithium plating in polymer electrolytes by concentration-polarization-induced phase transformation, Joule (2022), https://doi.org/10.1016/j.joule.2022.08.001

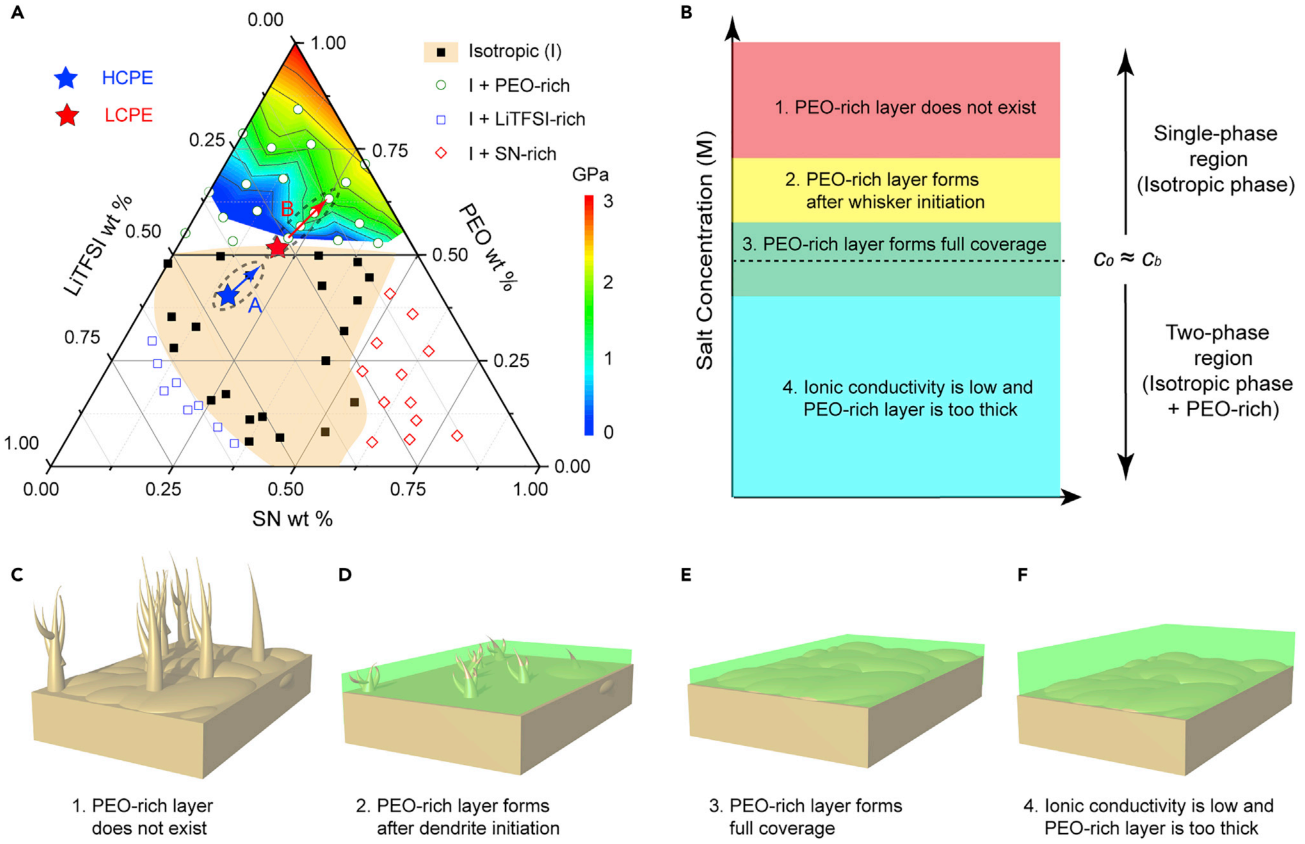

Figure 3. The phase diagram and the phase-diagram-derived design principle

(A) The ternary PEO-LiTFSI-SN phase diagram in weight percentage. The orange color marks the region of the isotropic single-phase region, while other regions represent two-phase regions. The rainbow color at the top of the triangle is the contour of Young's moduli of as-formed PEO-rich phases at corresponding compositions in the phase diagram.

(B) The schematic of how the initial salt concentration in a polymer electrolyte affects the thickness and the coverage of the PEO-rich layer when a current is applied.

(C) When c_0 is high, there is no PEO-rich layer formed and lithium whisker is easy to form ($c_0 >> c_b$).

(D) c_0 is moderately higher than the c_b, so the whisker is usually formed earlier than the PEO-rich layer. This leads to the partial passivation of lithium whisker growth.

(E) The suggested concentration range ($c_0 \approx c_b$) can yield the best passivation effect of the PEO-rich phase on lithium metal.

(F) $c_0 < c_b$, which has a low ionic conductivity and may result in a thick PEO-rich layer.

composition of HCPE is at the center of the I-zone. When a current is applied, it progressively decreases [LiTFSI] on the lithium metal surface (path A in Figure 3A). Due to the high salt concentration in HCPE, the electrolyte composition at the Li/electrolyte interface remains within the I-zone during concentration polarization, and thus no phase transformation occurred.

In contrast, the composition of LCPE is very close to the boundary between the single-phase I-zone and the two-phase region (c_b), making it susceptible to undergoing a phase transformation in response to concentration polarization (path B in Figures 3A and 3E), as forming two phases is thermodynamically more stable than staying in one phase. A lower t_+ can trigger phase evolution at an earlier time due to a larger ionic concentration gradient. This phase transformation decreases not only [LiTFSI] but also [SN] in the new phase (Video S3; Figures S9 and S10) because the PEO-rich phase also contains less SN, as indicated by Figure 3A. Moreover, the decreasing [SN] in the PEO-rich layer also repels SN into the bulk isotropic

Please cite this article in press as: Cheng et al., Stabilizing lithium plating in polymer electrolytes by concentration-polarization-induced phase transformation, Joule (2022), https://doi.org/10.1016/j.joule.2022.08.001

electrolyte, causing the accumulation of SN outside the PEO-rich layer (Figures S9 and S10). Such phenomena indicate that the redistribution of SN is a result of phase transformation instead of electromigration.

We further tested a Li/Li cell with EO:Li:SN = 8:1:2.64, where salt concentration was moderately higher than c_b. After lithium deposition started, lithium whiskers grew first and no PEO-rich phase was observed (Video S4). However, when the salt concentration on the lithium surface gradually decreased to be lower than c_b, the PEO-rich phase appeared and thickened, which suppressed lithium whisker growth. Nevertheless, the lithium surface could not be fully covered by the PEO-rich phase due to initially formed needle-like lithium whiskers, so the effectiveness of protection was undermined.

Finally, a polymer electrolyte with a concentration of 0.52 M LiTFSI and 2.6 M SN, which is deep inside the two-phase region, was also tested. This solid electrolyte, along with many other electrolytes deep inside the two-phase region, has a low ionic conductivity (0.02 mS cm^{-1}), which cannot afford a reasonable current density (e.g., >0.3 mA cm^{-2}) for normal operation. To cycle cells with such an electrolyte, the current density in this experiment is only 0.1 mA cm^{-2} for 1 h, and we have observed the same phase-evolution phenomena on the lithium metal surface (Video S5).

From the four cases above, we can conclude that the PEO-rich layer originates from solid phase transformation at or near RT, and its formation highly depends on salt concentration in the PEO electrolyte (Figure 3B). If the initial salt concentration (c_0) is deep inside the single-phase region as HCPE ($c_0 >> c_b$), the PEO-rich phase is unlikely to form (Figure 3C). If c_0 is moderately higher than c_b, whiskers may initiate before the formation of the PEO-rich phase, so the whisker growth cannot be fully suppressed (Figure 3D). If c_0 is close to c_b, such as LCPE, even a small current can form the PEO-rich phase that fully covers the lithium surface within a short period and effectively suppresses whiskers (Figure 3E). If $c_0 < c_b$, the ionic conductivity of the polymer electrolyte is usually low. In addition, the PEO-rich phase is readily formed on a lithium metal surface, but it may be too thick to conduct ions (Figure 3F).

Based on the analyses above, we propose a design principle of polymer electrolytes for LMBs: electrolyte composition should be at the boundary between the single-phase and two-phase regions in the PEO-salt-plasticizer phase diagram so that a small current induces reduced salt concentration and forms a mechanically strong PEO-rich phase on the lithium metal surface. To further support our proposal, we determined another LCPE electrolyte from the phase diagram in Figure 3A, which has a composition of EO:Li:SN = 17.1:1:5.66, 50% more SN than the one we previously used. As shown in Video S6, even with a higher portion of SN, the PEO-rich layer can still form on the lithium metal surface and suppress the growth of lithium whiskers.

Mechano-chemical coupling in PEO-rich layer and mechanisms of whisker suppression

The effective suppression of Li whiskers by this new PEO-rich phase is hypothesized to arise from mechano-chemical coupling during the phase transformation at the Li/electrolyte interface. To verify this, AFM was used to measure Young's moduli of SPEs with different compositions, including both the isotropic phase (I-zone) and the PEO-rich phase, and the results are superimposed onto the phase diagram in Figure 3A. For the composition of the HCPE (1.8 M LiTFSI and 2.4 M SN), the

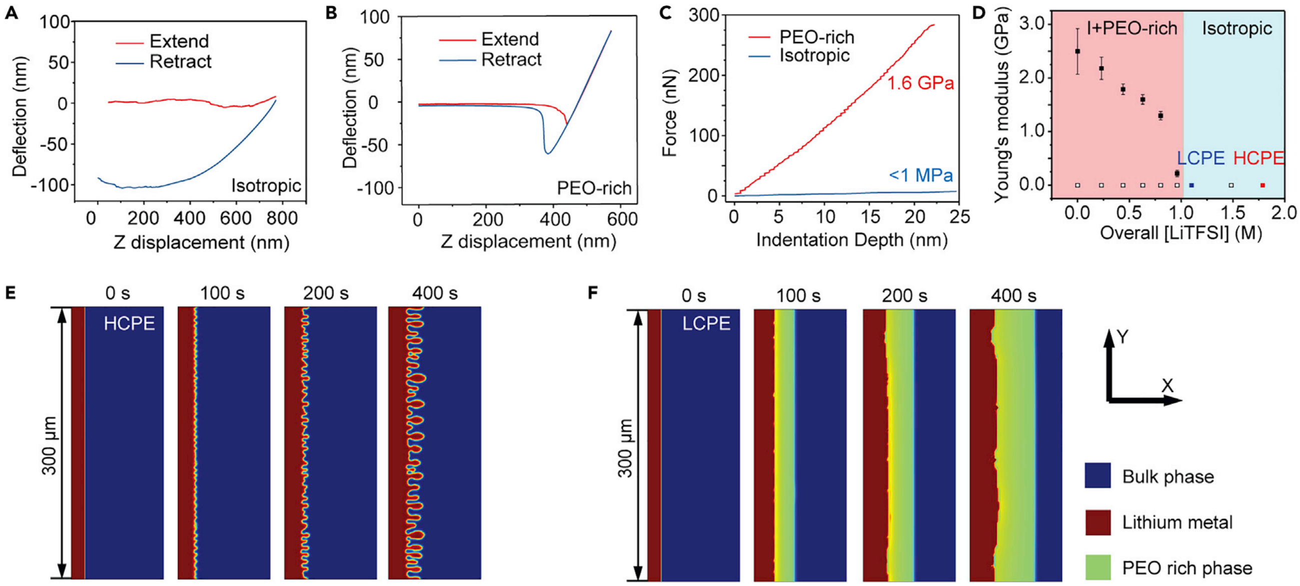

Figure 4. The mechanical properties of PEO-LiTFSI-SN polymer electrolytes and the phase-field simulations

(A and B), the AFM extending and retraction force curves of (A). The isotropic bulk phase (I-zone, HCPE). No cantilever deformation was detected. (B) The as-formed PEO-rich phase with a composition of 0.52 M LiTFSI and 2.6 M SN (see Table S5 for details).

(C) The corresponding force-indentation curves for samples in (A) and (B).

(D) Young's moduli of the PEO-rich phase with different salt concentrations. Error bars represent standard deviation. The sample compositions are along the path A and B in Figure 3A. All samples have the same SN/PEO ratio as HCPE and LCPE (40 wt %), but different [LiTFSI]. The exact composition of each phase is listed in Table S4. The solid and empty squares show Young's moduli of the PEO-rich phase and the isotropic bulk phases, respectively.

(E and F) Phase-field simulations of lithium electrodeposition in solid polymer electrolytes with (E) a high concentration (2 M salt) and (F) a low concentration (1 M salt) at 0.5 mA cm^{-2}.

approaching curve showed no deformation of the cantilever when the tip was pressed into the electrolyte, indicating that the electrolyte was very soft (Figure 4A). Large cantilever deflection was detected during tip retraction, confirming that the tip was pressed inside HCPE and that the electrolyte was sticky. All SPEs within the I-zone and the isotropic phase of SPEs in the two-phase regions in Figure 3A displayed similar results (Young's modulus < 1 MPa), indicating they could not mechanically suppress lithium whisker growth.

Conversely, a classic force curve was observed for the PEO-rich phase formed in SPE. The sample had an overall composition of 0.6 M LiTFSI and 3.3 M SN, and the PEO-rich phase inside contained 0.52 M LiTFSI and 2.6 M SN (Figure 4B). The conductivity of the as-formed PEO-rich state is in the order of 10^{-5} S cm^{-1} as there is still a reasonable amount of LiTFSI (0.2–0.6 M) and SN (2–3 M) left inside, which still allows Li^+ to shuttle (Figure S11). Using the Sneddon model,[53] the corresponding modulus was 1.6 GPa (Figure 4C) and the indentation hardness ~410–780 MPa (Table S5; Note S6). The indentation hardness of a material is usually 3 times its tensile strength, implying that the PEO-rich phase's tensile strength is ~137 MPa. Such stress is well beyond the hardness (~7–43 MPa) and yield strength (0.6–1.3 MPa) of lithium metal reported in the literature,[54] so the creep of lithium metal is inevitable during lithium deposition, which results in the suppression of lithium whisker growth (see Note S6 for detailed analysis). In contrast, the bulk PEO electrolyte has a modulus < 1 MPa, similar to or smaller than the hardness and the yield strength of lithium metal, so lithium whisker growth cannot be suppressed. In addition, such analysis is also consistent with previous studies[24] explaining why whisker growth was suppressed in LCPE.

Please cite this article in press as: Cheng et al., Stabilizing lithium plating in polymer electrolytes by concentration-polarization-induced phase transformation, Joule (2022), https://doi.org/10.1016/j.joule.2022.08.001

To further understand mechano-chemical coupling at the Li/electrolyte interface, the composition-dependent mechanical properties of the PEO-rich phases in PEO electrolytes were systematically measured by AFM. As shown in Figure 4D, the moduli of the PEO-rich phases quickly rise to 1.2–1.8 GPa when [LiTFSI] is reduced to 0.80 and 0.44 M in the PEO-rich phase, respectively (Table S5). Further contour on Young's moduli of the PEO-rich phases in the I + PEO-rich two-phase region (Figure 3A) shows that the modulus is typically above 1 GPa when [LiTFSI] is less than 0.8 M. Because pure crystalline PEO has a Young's modulus of 5–7 GPa,[55,56] it is reasonable that a semi-crystalline PEO-rich layer with a limited amount of salt/plasticizer inside can reach a modulus of 1–2 GPa. The contour indicates that the mechanism of concentration-polarization-induced stabilization of lithium deposition is effective in a wide range of electrolyte compositions.

The proposed suppression mechanism is also supported by the phase-field simulation, which takes the mechano-chemical coupling into account (Note S7; Video S7). Based on the results above, the simulation assumed that the PEO-rich phase formed when overall [LiTFSI] was < 0.85 M and the PEO-rich phase had Young's modulus of 1.6 GPa, while any region with [LiTFSI] ≥ 0.85 M had a modulus of <1 MPa. Because no new phase was formed in the HCPE, lithium whiskers grew fast in the soft isotropic bulk polymer electrolyte (Figures 4E and S17A). In contrast, the PEO-rich phase was formed once [Li^+] was polarized to below 0.85 M, effectively suppressing lithium whisker growth (Figures 4F and S17B). The deposited lithium was widely uniform and the [Li^+] heterogeneity was low on the lithium surface. These simulation results strongly agree with experimental observations, supporting the hypothesis that the formation of the PEO-rich phase with high Young's modulus suppresses whisker growth.

In addition, our results do not conflict with Chazelviel's previous work,[57,58] where cells were operated at the molten state (80°C) and dendrites grew faster at full ion depletion. In our case, the polymer electrolyte is solid (RT), and phase transformation exists upon the decrease of salt concentration so that a mechanically rigid PEO-rich phase forms and suppresses whisker growth. The salt concentration does not decrease to 0 M and thus it avoids the formation of the space charge region, which induces the ultrahigh electrical field and dendrite growth. In addition, we consider the observed phase transformation as a method to enhance the suppression of lithium whisker growth, but not a method that can eliminate whisker/dendrite growth.

Concentration-polarization-induced stabilization of Li anode in Li/Li and LFP/PEO/Li cells

With the understanding that the formation of a mechanically rigid PEO-rich phase can stabilize lithium deposition, and that an electrolyte with composition at the boundary between single-phase and two-phase regions can induce the formation of such a PEO-rich phase, we further examined the effectiveness of this strategy in repeated cycles in Li/Li cells and full cells.

First, as a proof-of-concept experiment, a current of 0.5 mA cm^{-2} was applied to a Li/SN-LCPE/Li symmetrical cell with a deposition capacity of 0.25 mAh cm^{-2} for 20 cycles at RT. As observed from the optical microscope (Figure 5A; Video S8), no obvious lithium whiskers formed in the first deposition, and the lithium protrusions were frozen by the growing PEO-rich phase, leading to stable lithium deposition. During lithium stripping, both the PEO-rich phase and lithium metal electrode shrank without forming any dead lithium debris. The lithium surface moved forward

Please cite this article in press as: Cheng et al., Stabilizing lithium plating in polymer electrolytes by concentration-polarization-induced phase transformation, Joule (2022), https://doi.org/10.1016/j.joule.2022.08.001

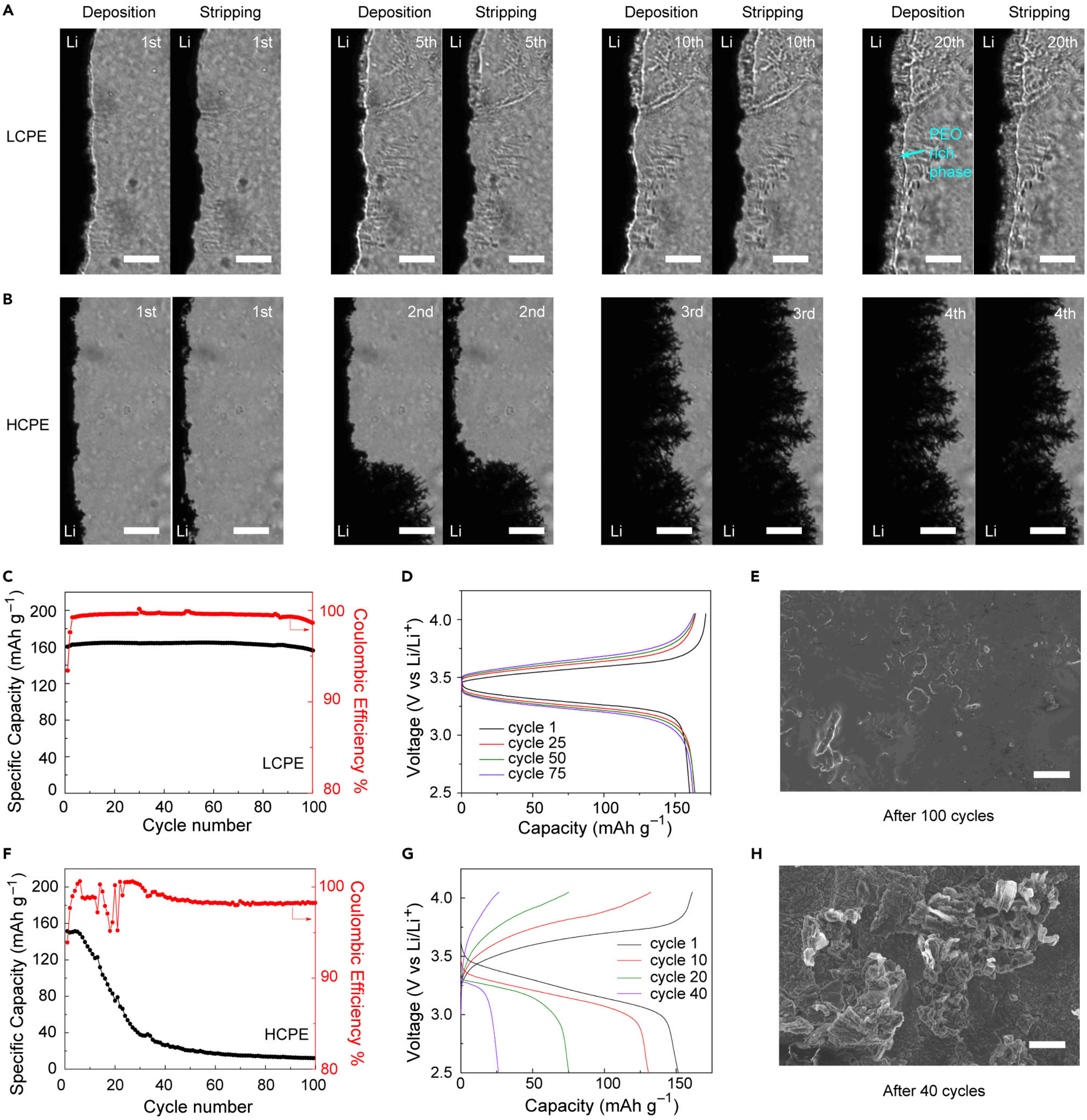

Figure 5. Cycling stability of the lithium metal anode in LCPE and HCPE

(A and B) The bright-field images of the lithium electrodes during lithium plating and stripping with a current density of 0.5 mA cm^{-2} in (A) LCPE and (B) HCPE. The scale bars are 100 μm.

(C and D) (C) The cycling performance of a LiFePO$_4$/Li battery with LCPE, and (D) the corresponding voltage profiles.

(E) An SEM image of the lithium metal surface after 100 cycles.

(F and G) (F) The cycling of LiFePO$_4$/Li metal battery with HCPE and (G) the corresponding voltage profiles.

(H) An SEM image of the lithium metal surface after 40 cycles. The scale bars in (E) and (H) are 10 μm. The current densities for both batteries are 0.15 mA cm^{-2}. All cells were tested at 40°C.

slightly after 20 cycles, indicating that this suppression mechanism was effective upon multiple cycles.

Such a reversible behavior is universal, and it could be achieved in a wide range of currents from 0.1 to 1 mA cm^{-2} for LCPE (Video S8; Figure S18), where the corresponding limiting current was 0.28 mA cm^{-2} (Note S5; Figure S12). It should be noted that the PEO-rich phase sometimes did not fully disappear during lithium stripping, which was attributed to its disappearance being a kinetically slow process. In contrast, without the PEO-rich phase, fast whisker growth was observed within the first several cycles for Li/Li cells with HCPE, forming large amounts of dead lithium during the repeated stripping process (Figure 5B; Video S8). The voltage polarization also increased in a few cycles of plating and stripping due to the formation of dead lithium (Figure S19).

To show that the formation of the PEO-rich phase in LCPE does not depend on the current density, we prepared Li/Li cells with a more practical electrolyte width of 150 μm and cycled them with a small current density of 0.1 mA cm^{-2}, which is well below the limiting current density of 0.8 mA cm^{-2}. The PEO-rich phase still formed in deposition and dissolved in stripping reversibly (Video S9; Figure S20), proving that a low current density well below the limiting current density could still trigger the formation of the PEO-rich phase if the electrolyte composition were chosen at the boundary between the single-phase and two-phase regions.

We further assembled Li/Cu cells to validate that the corresponding CE was reasonable. The cells were cycled at 0.1 mA cm^{-2} for 4 h. For LCPE, the initial CE was around 90% and it was stabilized at 92%–95% after ~40 cycles (Figure S21A). The overpotential of lithium plating and stripping also barely changed within 40 cycles (Figure S21B). These results indicate that the LCPE-based electrolyte results in stable lithium deposition instead of side reactions. In contrast, the HCPE cell has a fluctuating CE between 70% and 90% as a result of whisker formation. The overpotential also increased after 40 cycles, showing the possible accumulation of dead lithium on the electrode (Figure S21C).

The effectiveness of this strategy was also demonstrated in LFP/PEO/Li cells at 0.25 C and 40°C. LFP cathodes with a mass loading of ~4 mg cm^{-2} were assembled with PEO electrolytes and lithium metal. The thickness of the PEO electrolyte was fixed at 100 μm without using a separator (Figure S22). Stable cycling was achieved with LCPE. The initial discharge capacity was 160.2 mAh g^{-1} with a CE of 93.4% and slowly increased to 164.2 mAh g^{-1} in the 10th cycle as a result of activation. After 100 cycles, the capacity remained at 156.1 mAh g^{-1}, corresponding to retention of 97.4%. The average CE from the 5th cycle to the 100th cycle was 99.5% (Figure 5C). The voltage profile shows that the internal resistance only increases slightly, and there is no sign of a whisker-induced short circuit (Figure 5D). SEM further revealed that the lithium metal surface was relatively flat after 100 cycles, with occasional island-like morphology, demonstrating the effectiveness of the PEO-rich phase in suppressing lithium whiskers (Figure 5E).

On the other hand, the LFP/PEO/Li cell with HCPE quickly failed, with the capacity dropping from 151.5 to 26.2 mAh g^{-1} after 40 cycles (Figure 5F). The voltage profile showed a drastically increased overpotential, which suggests possible whisker growth (Figure 5G). The average CE is only 98.2%, which probably arises from the prosperous growth of lithium whiskers, as validated by the SEM image (Figure 5H).

Please cite this article in press as: Cheng et al., Stabilizing lithium plating in polymer electrolytes by concentration-polarization-induced phase transformation, Joule (2022), https://doi.org/10.1016/j.joule.2022.08.001

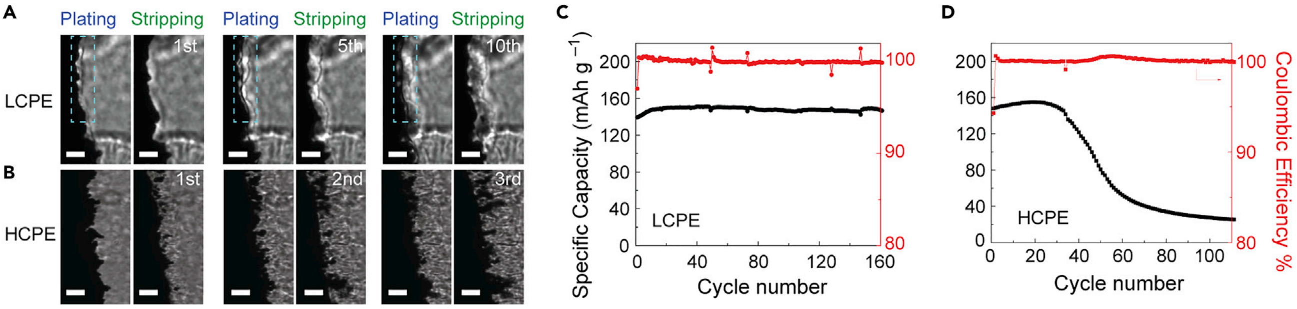

Figure 6. Cycling stability of the lithium metal anode in Li/Li cells and LFP/Li cells with PC/LiDFOB-LiBF$_4$ dual salt-based LCPE and HCPE

(A and B) The bright-field images of the lithium electrodes in Li/Li cells with (A) LCPE and (B) HCPE at room temperature and 0.75 mA cm^{-2}. The scale bars are 25 μm to better show the as-formed new PEO-rich phase (the dashed blue area).

(C and D) The cycling performance of LiFePO$_4$/Li metal batteries with (C) LCPE and (D) HCPE at 38°C. The current density is 0.3 mA cm^{-2}. In LCPE, PEO:LiDFOB:LiBF$_4$ = 12:1:1, and PC is 90 wt % of PEO. In HCPE, PEO:LiDFOB:LiBF$_4$ = 6:1:1, and PC is 90 wt % of PEO.

More reproducible results can be found in Figure S23. The charge transfer resistance (R_{ct}) further supports the conclusion. The R_{ct} of LCPE and HCPE increase 77% and 132%, respectively (Figures S24A and S24B; Table S6), further proving the formation of mossy lithium and dead lithium in the cells with HCPE.

Such phase-separation-induced whisker suppression is universal in PEO electrolytes. In another lithium difluoro(oxalato)borate (LiDFOB) and lithium tetrafluoroborate (LiBF$_4$) in PEO/propylene carbonate (PC) plasticizer system, a similar phenomenon was also observed. We first identify the boundary of the single-phase region and two-phase regions in this system, which is at EO:Li$^+$ = 6 with a conductivity of 2.9 mS cm^{-1} (PC-LCPE, Figure S25). Hence, Li/Li cells were tested with PC-LCPE at 0.75 and 0.375 mAh cm^{-2} and characterized using an optical microscope. A PEO-rich layer was observed during lithium deposition and was capable of suppressing lithium whiskers (Figures 6A and S26; Video S10). In contrast, phase separation was not observed in the PC-HCPE with EO/Li$^+$ = 3 (5.2 mS cm^{-1}), and obvious whiskers and dead lithium were formed (Figure 6B). The effectiveness of the strategy was also demonstrated in full cells at 40°C, where both films are still solid and free-standing (Figure S27). In an LFP/PC-LCPE/Li cell with 5 mg LFP cm^{-2} and 40 μm thin lithium (Figure 6C), the cell showed steady cycling over 160 cycles at 0.3 mA cm^{-2} (139.4, 149.9, and 147.1 mAh g^{-1} in cycle 1, 25, and 160, respectively). In contrast, when PC-LCPE was replaced by PC-HCPE, the cell only has capacity retention of 17.3% after 100 cycles (Figure 6D). The corresponding voltage profiles are shown in Figure S28. Similar to SN-based electrolytes, The R_{ct} increase of LCPE is much smaller than that of HCPE (Figures S24C and S24D; Table S6). More reproduced results are in Figure S29. Batteries with 10 mg LFP cm^{-2} (1.3 mAh cm^{-2}) and 40 μm lithium foil also showed stable cycling. The cell capacity was 116 mAh g^{-1} in cycle 1, 131 mAh g^{-1} in cycle 20, and 119 mAh g^{-1} in cycle 80 (Figure S30). These results of SN-LCPE and PC-LCPE polymer electrolytes are among the best at a similar temperature (30°C–40°C) in literature (Table S7; Figure S31), showing that stable lithium plating can be achieved in polymer electrolytes by optimizing the salt concentration.

Such concentration-polarization-induced phase transformation also exists in polymer electrolytes without plasticizer or with a different polymer host. We imaged Li/Li cells with a polyethylene oxide (Mw =1,500)/LiTFSI electrolyte and a polyethylene glycol diacrylate/SN/LiTFSI electrolyte. When a current is applied, a secondary

Please cite this article in press as: Cheng et al., Stabilizing lithium plating in polymer electrolytes by concentration-polarization-induced phase transformation, Joule (2022), https://doi.org/10.1016/j.joule.2022.08.001

phase can be observed on the surface of lithium plating in both cases, further validating this phenomenon (Videos S11 and S12).

DISCUSSION

The dynamic concentration polarization, phase transformation in polymer electrolytes, and their correlations with lithium deposition were observed for the first time thanks to the high chemical, temporal, and spatial resolutions of SRS microscopy. We successfully unveiled phase transformation in polymer electrolytes induced by concentration polarization and the formation of a new PEO-rich phase at electrode/electrolyte interface. Such a phase transformation exists in various other polymer electrolyte systems (Videos S11 and S12). This new phase has a high Young's modulus of up to 3 GPa, which is effective in mechanically suppressing lithium whisker growth by functioning as a reversible, self-reinforcing protective layer on a lithium anode. In contrast, without such phase transformation, conventional polymer electrolytes have a small modulus < 1 MPa, leading to fast lithium whisker growth. Based on such understanding, we proposed a design rule for polymer electrolytes:electrolyte composition should be at the boundary between the single-phase and the two-phase regions in the PEO-salt-plasticizer phase diagram so that current can easily reduce salt concentration on lithium metal surfaces and lead to the formation of the PEO-rich phase on the lithium metal surface.

By utilizing this design rule, we successfully demonstrated LFP/PEO/Li cells with stable cycling, while cells without this mechanism failed quickly within 10 cycles. This strategy is also compatible with state-of-the-art battery materials and manufacturing process, without the extra need to control the conformability of protective layers. Moreover, the strategy is universal and effective with different salt and plasticizers, and it facilitates the development of solid polymer-electrolyte-based LMBs with enhanced thermal stability and high energy density. It should be mentioned that extra polarization brought by the new phase requires discreet design on parameters such as film thickness and salt concentration. Meanwhile, although this strategy helps enhance the suppression of lithium whisker growth, it is unlikely to eliminate the uneven growth of lithium, especially in harsher conditions, and should be combined with other strategies for further improving the reversible plating/stripping of lithium metal. In the future, the ion concentration profile and possible phase evolution in cross-linked polymers and polymers with ceramic fillers require more investigation using SRS, and would further help design polymer electrolytes with better performance.[59] The phase evolution discovered in this work may help in understanding and designing polymer electrolytes in other electrochemical systems, and optimize the composition to achieve better performance. For example, the asymmetric composition induced by phase evolution may be helpful for designing ionic diodes and thermogalvanic cells.[60]

EXPERIMENTAL PROCEDURES

Resource availability

Lead contact

Further information and requests for resources and materials should be directed to and will be fulfilled by the lead contact, Yuan Yang (yy2664@columbia.edu).

Materials availability

This study did not generate new unique materials.

Data and code availability

The data that support the plots within this this study are available from the corresponding authors upon requests.

Preparation of SPE precursors

To prepare SN-LCPE / HCPE, 0.19 g / 0.38 g LiTFSI (Gotion) was dissolved in 5 g acetonitrile (Sigma Aldrich) along with 0.35 g poly (ethylene oxide) (Mw 600,000, Sigma Aldrich) and 0.14 g SN (Tokyo Chemical Industry). Then the solution was stirred overnight to form a translucent solution. SPEs with other compositions were prepared similarly, and PEO is typically 7 wt % of acetonitrile. For PC-LCPE/HCPE, the preparation procedure is similar. LiDFOB and $LiBF_4$ are mixed first with a molar ratio of 1:1, then the dual salts, PEO, and PC with a weight of 0.16/0.32, 0.35, and 0.315 g, respectively, were dissolved in 5 g acetonitrile.

Preparation of the lithium-lithium symmetric cells

40 μm thick of lithium foil and 50 μm thick of SPEs were used in the Li/Li symmetric cells while the horizontal gap between two lithium metal electrodes is ~ 500 μm. One layer of Kapton tape was laminated onto a glass slide, and two chambers (~1 × 1 cm for each) and a channel (~1 × 6 mm) to connect two chambers were cut inside Kapton tapes (thickness ~ 100 μm). We tried to drop the PEO electrolyte onto the lithium surface at a high temperature and melt PEO to form a better Li/PEO interface. Unfortunately, there was still a high impedance, and the overpotential was very high even at a low current density. Therefore, PEO electrolyte was prepared *in situ* to form a low-resistance interface. The lithium foil was cut to the desired size and soaked in dimethyl sulfoxide (DMSO) with 0.2 wt % H_3PO_4 solution for 1 min to form a thin Li_3PO_4 protective layer to isolate the contact between Li and acetonitrile in the SPE precursor above. Lithium electrodes were then placed at two ends of the chamber, and the precursor of SPE above was dropped between two Li electrodes and rested to evaporate acetonitrile. Finally, Cu foils with similar sizes were placed on the two ends of lithium as an external electrical contact, and a glass cover was placed on top of the Li/Li cell, followed by sealing with epoxy. The whole process was done in a glove box with O_2 and water levels < 0.1 ppm.

Preparation of the LFP-PEO-Li cells

For SN-based PEO electrolyte, LFP was selected as the cathode material due to its stability with PEO electrolyte. LFP, carbon black, and polyvinylidene fluoride (PVDF) were mixed with a mass ratio of 8:1:1, then stirred in N-methyl-2-pyrrolidone (NMP) overnight to form a uniform slurry. Then the LFP slurry was coated on an Al foil using the doctor-blade method, followed by drying at 110°C for 12 h. The mass loading of LFP is ~ 4 mg cm^{-2}. Then the LFP electrodes were assembled with 40 μm lithium metal as anode and SN-LCPE/HCPE as the electrolyte in an argon-filled glove box with both H_2O and O_2 below 0.1 ppm. A Kapton ring with a thickness of 100 μm was used to fixate the distance between the LFP electrode and lithium metal. The cells were tested at 40°C, which enhanced ionic conductivity but the formation of the new PEO-rich phase still occurred. The cells were rested for 15 min and 1 h after each charging and discharging step, respectively.

For PC-based PEO electrolytes, the preparation procedure is similar, except that 0.7 wt % of carbon nanotubes (CNTs) were added into the LFP electrodes to achieve better rate performance at high mass loading (5–10 mg). The electrode will be infiltrated with PEO/PC/dual salts electrolyte first, then roll-pressed, and assembled with 40 μm thick lithium metal. The batteries were tested under 38°C.

SUPPLEMENTAL INFORMATION

Supplemental information can be found online at https://doi.org/10.1016/j.joule.2022.08.001.

ACKNOWLEDGMENTS

We acknowledge seed funding support from Columbia University's Research Initiatives in Science & Engineering competition, which started in 2004 to trigger high-risk, high-reward, and innovative collaborations in the basic sciences, engineering, and medicine. Y.Y., Q.C., and T.J. acknowledge the support from the Air Force Office of Scientific Research (FA9550-18-1-0410 and FA9550-20-1-0233). W.M. and Y.M. acknowledge the support from National Science Foundation (grant no. 1904684). L.-Q.C. and Z.L. acknowledge the support from the Department of Energy, Office of Energy Efficiency and Renewable Energy (EERE), under the award #DE-EE0007803 from the Battery Material Research (BMR) program. X.C. and H.W. are thankful for the support of the Office of Naval Research (ONR) under grant no. N00014-18-1-2492 and Army Research Office (ARO) under grant no. W911NF-21-1-0172. J.L. acknowledges support by NSF CBET-2034902. S.-Y.K. gratefully acknowledges partial financial support by the Kwanjeong Scholarship. We also want to thank Prof. William Goddard at Caltech and Dr. Steve Harris at Lawrence berkeley national laboratory for their kind suggestions to this work.

AUTHOR CONTRIBUTIONS

Q.C., T.J., and Y.M. contributed equally to this work. Conceptualization, Y.Y., W.M., and Q.C.; methodology, Y.Y., W.M., Q.C., Z.L., and L.-Q.C.; investigation, Q.C. and Y.M.; validation, T.J.; formal analysis, Q.C., Y.M., H.Z., J.B., S.-Y.K., J. L., S.L., H.W., and X.C.; writing – original draft, Q.C. and Y.M.; writing – review & editing, Q.C., T.J., Y.Y., W.M., and R.Z.; funding acquisition, Y.Y., W.M., L.Q.-C., and X.C.; supervision, Y.Y. and W.M.

DECLARATION OF INTERESTS

The authors declare no competing interests.

Received: January 24, 2022
Revised: July 11, 2022
Accepted: August 9, 2022
Published: September 2, 2022

REFERENCES

1. Cheng, X.-B., Zhang, R., Zhao, C.-Z., and Zhang, Q. (2017). Toward safe lithium metal anode in rechargeable batteries: a review. Chem. Rev. *117*, 10403–10473.
2. Lin, D., Liu, Y., and Cui, Y. (2017). Reviving the lithium metal anode for high-energy batteries. Nat. Nanotechnol. *12*, 194–206.
3. Albertus, P., Babinec, S., Litzelman, S., and Newman, A. (2018). Status and challenges in enabling the lithium metal electrode for high-energy and low-cost rechargeable batteries. Nat. Energy *3*, 16–21.
4. Li, N.W., Yin, Y.X., Yang, C.P., and Guo, Y.G. (2016). An artificial solid electrolyte interphase layer for stable lithium metal anodes. Adv. Mater. *28*, 1853–1858.
5. Basile, A., Bhatt, A.I., and O'Mullane, A.P. (2016). Stabilizing lithium metal using ionic liquids for long-lived batteries. Nat. Commun. *7*. ncomms11794.
6. Han, F., Westover, A.S., Yue, J., Fan, X., Wang, F., Chi, M., Leonard, D.N., Dudney, N.J., Wang, H., and Wang, C. (2019). High electronic conductivity as the origin of lithium dendrite formation within solid electrolytes. Nat. Energy *4*, 187–196.
7. Wang, X., Zeng, W., Hong, L., Xu, W., Yang, H., Wang, F., Duan, H., Tang, M., and Jiang, H. (2018). Stress-driven lithium dendrite growth mechanism and dendrite mitigation by electroplating on soft substrates. Nat. Energy *3*, 227–235.
8. Xiao, J. (2019). How lithium dendrites form in liquid batteries. Science *366*, 426–427.
9. Liu, J., Bao, Z., Cui, Y., Dufek, E.J., Goodenough, J.B., Khalifah, P., Li, Q., Liaw, B.Y., Liu, P., Manthiram, A., et al. (2019). Pathways for practical high-energy long-cycling lithium metal batteries. Nat. Energy *4*, 180–186.
10. Xu, K. (2004). Nonaqueous liquid electrolytes for lithium-based rechargeable batteries. Chem. Rev. *104*, 4303–4417.
11. Tikekar, M.D., Choudhury, S., Tu, Z., and Archer, L.A. (2016). Design principles for electrolytes and interfaces for stable lithium-metal batteries. Nat. Energy *1*, 16114.

Please cite this article in press as: Cheng et al., Stabilizing lithium plating in polymer electrolytes by concentration-polarization-induced phase transformation, Joule (2022), https://doi.org/10.1016/j.joule.2022.08.001

12. Ren, X., Chen, S., Lee, H., Mei, D., Engelhard, M.H., Burton, S.D., Zhao, W., Zheng, J., Li, Q., Ding, M.S., et al. (2018). Localized high-concentration sulfone electrolytes for high-efficiency lithium-metal batteries. Chem *4*, 1877–1892.
13. Chen, S., Zheng, J., Mei, D., Han, K.S., Engelhard, M.H., Zhao, W., Xu, W., Liu, J., and Zhang, J.G. (2018). High-voltage lithium-metal batteries enabled by localized high-concentration electrolytes. Adv. Mater. *30*, e1706102.
14. Lu, Q., He, Y.B., Yu, Q., Li, B., Kaneti, Y.V., Yao, Y., Kang, F., and Yang, Q.H. (2017). Dendrite-free, High-Rate, long-life lithium metal batteries with a 3D cross-linked network polymer electrolyte. Adv. Mater. *29*, 1604460.
15. Panday, A., Mullin, S., Gomez, E.D., Wanakule, N., Chen, V.L., Hexemer, A., Pople, J., and Balsara, N.P. (2009). Effect of molecular weight and salt concentration on conductivity of block copolymer electrolytes. Macromolecules *42*, 4632–4637.
16. Stone, G.M., Mullin, S.A., Teran, A.A., Hallinan, D.T., Minor, A.M., Hexemer, A., and Balsara, N.P. (2012). Resolution of the modulus versus adhesion dilemma in solid polymer electrolytes for rechargeable lithium metal batteries. J. Electrochem. Soc. *159*, A222–A227.
17. Hess, S., Wohlfahrt-Mehrens, M., and Wachtler, M. (2015). Flammability of Li-ion battery electrolytes: flash point and self-extinguishing time measurements. J. Electrochem. Soc. *162*, A3084–A3097.
18. Li, D., Fang, W., Xing, Y., Guo, Y., and Lin, R. (2009). Effects of dimethyl or diethyl carbonate as an additive on volatility and flash point of an aviation fuel. J. Hazard. Mater. *161*, 1193–1201.
19. Catoire, L., and Naudet, V. (2004). A unique equation to estimate flash points of selected pure liquids application to the correction of probably erroneous flash point values. J. Phys. Chem. Ref. Data *33*, 1083–1111.
20. Li, S., Chen, Y.-M., Liang, W., Shao, Y., Liu, K., Nikolov, Z., and Zhu, Y. (2018). A superionic conductive, electrochemically stable dual-salt polymer electrolyte. Joule *2*, 1838–1856.
21. Maitra, M.G., Sinha, M., Mukhopadhyay, A.K., Middya, T.R., De, U., and Tarafdar, S. (2007). Ion-conductivity and Young's modulus of the polymer electrolyte PEO–ammonium perchlorate. Solid State Ion *178*, 167–171.
22. Geng, H.Z., Rosen, R., Zheng, B., Shimoda, H., Fleming, L., Liu, J., and Zhou, O. (2002). Fabrication and properties of composites of poly (ethylene oxide) and functionalized carbon nanotubes. Adv. Mater. *14*, 1387–1390.
23. Klongkan, S., and Pumchusak, J. (2015). Effects of nano alumina and plasticizers on morphology, ionic conductivity, thermal and mechanical properties of PEO-$LiCF_3SO_3$ solid polymer electrolyte. Electrochim. Acta *161*, 171–176.
24. Barai, P., Higa, K., and Srinivasan, V. (2017). Lithium dendrite growth mechanisms in polymer electrolytes and prevention strategies. Phys. Chem. Chem. Phys. *19*, 20493–20505.
25. Brissot, C., Rosso, M., Chazalviel, J.-N., and Lascaud, S. (1999). *In situ* concentration cartography in the neighborhood of dendrites growing in lithium/polymer-electrolyte/lithium cells. J. Electrochem. Soc. *146*, 4393–4400.
26. Liu, S., Imanishi, N., Zhang, T., Hirano, A., Takeda, Y., Yamamoto, O., and Yang, J. (2010). Effect of nano-silica filler in polymer electrolyte on Li dendrite formation in Li/poly (ethylene oxide)–Li $(CF_3SO_2)\ _2N$/Li. J. Power Sources *195*, 6847–6853.
27. Ramesh, S., Winie, T., and Arof, A.K. (2007). Investigation of mechanical properties of polyvinyl chloride–polyethylene oxide (PVC–PEO) based polymer electrolytes for lithium polymer cells. Eur. Polym. J. *43*, 1963–1968.
28. Fu, K.K., Gong, Y., Dai, J., Gong, A., Han, X., Yao, Y., Wang, C., Wang, Y., Chen, Y., Yan, C., et al. (2016). Flexible, solid-state, ion-conducting membrane with 3D garnet nanofiber networks for lithium batteries. Proc. Natl. Acad. Sci. USA *113*, 7094–7099.
29. Zeng, X., Li, M., Abd El-Hady, D., Alshitari, W., Al-Bogami, A.S., Lu, J., and Amine, K. (2019). Commercialization of lithium battery technologies for electric vehicles. Adv. Energy Mater. *9*, 1900161.
30. Fang, C., Li, J., Zhang, M., Zhang, Y., Yang, F., Lee, J.Z., Lee, M.-H., Alvarado, J., Schroeder, M.A., Yang, Y., et al. (2019). Quantifying inactive lithium in lithium metal batteries. Nature *572*, 511–515.
31. Li, Y., Li, Y., Pei, A., Yan, K., Sun, Y., Wu, C.-L., Joubert, L.M., Chin, R., Koh, A.L., Yu, Y., et al. (2017). Atomic structure of sensitive battery materials and interfaces revealed by cryo-electron microscopy. Science *358*, 506–510.
32. Zachman, M.J., Tu, Z., Choudhury, S., Archer, L.A., and Kourkoutis, L.F. (2018). Cryo-STEM mapping of solid-liquid interfaces and dendrites in lithium-metal batteries. Nature *560*, 345–349.
33. Bhattacharyya, R., Key, B., Chen, H., Best, A.S., Hollenkamp, A.F., and Grey, C.P. (2010). *In situ* NMR observation of the formation of metallic lithium microstructures in lithium batteries. Nat. Mater. *9*, 504–510.
34. Chandrashekar, S., Trease, N.M., Chang, H.J., Du, L.-S., Grey, C.P., and Jerschow, A. (2012). ^7Li MRI of Li batteries reveals location of microstructural lithium. Nat. Mater. *11*, 311–315.
35. Xu, S., Sun, Z., Sun, C., Li, F., Chen, K., Zhang, Z., Hou, G., Cheng, H.M., and Li, F. (2020). Homogeneous and fast ion conduction of PEO-based solid-state electrolyte at low temperature. Adv. Funct. Mater. *30*, 2007172.
36. Chen, Y., Wang, Z., Li, X., Yao, X., Wang, C., Li, Y., Xue, W., Yu, D., Kim, S.Y., Yang, F., et al. (2020). Li metal deposition and stripping in a solid-state battery via Coble creep. Nature *578*, 251–255.
37. Yan, Y., Cheng, C., Zhang, L., Li, Y., and Lu, J. (2019). Deciphering the reaction mechanism of lithium–sulfur batteries by *in situ*/*operando* synchrotron-based characterization techniques. Adv. Energy Mater. *9*, 1900148.
38. Cao, C., Shyam, B., Wang, J., Toney, M.F., and Steinrück, H.G. (2019). Shedding X-ray light on the interfacial electrochemistry of silicon anodes for Li-ion batteries. Acc. Chem. Res. *52*, 2673–2683.
39. Yu, S.-H., Huang, X., Brock, J.D., and Abruña, H.D. (2019). Regulating key variables and visualizing lithium dendrite growth: an operando X-ray study. J. Am. Chem. Soc. *141*, 8441–8449.
40. Steinrück, H.-G., Takacs, C.J., Kim, H.-K., Mackanic, D.G., Holladay, B., Cao, C., Narayanan, S., Dufresne, E.M., Chushkin, Y., Ruta, B., et al. (2020). Concentration and velocity profiles in a polymeric lithium-ion battery electrolyte. Energy Environ. Sci. *13*, 4312–4321.
41. Cheng, Q., Wei, L., Liu, Z., Ni, N., Sang, Z., Zhu, B., Xu, W., Chen, M., Miao, Y., Chen, L.Q., et al. (2018). *Operando* and three-dimensional visualization of anion depletion and lithium growth by stimulated Raman scattering microscopy. Nat. Commun. *9*, 2942.
42. Fleury, G., Steele, J.A., Gerber, I.C., Jolibois, F., Puech, P., Muraoka, K., Keoh, S.H., Chaikittisilp, W., Okubo, T., and Roeffaers, M.B.J. (2018). Resolving the framework position of organic structure-directing agents in hierarchical zeolites via polarized stimulated Raman scattering. J. Phys. Chem. Lett. *9*, 1778–1782.
43. Li, H., Cheng, Y., Tang, H., Bi, Y., Chen, Y., Yang, G., Guo, S., Tian, S., Liao, J., Lv, X., et al. (2020). Imaging chemical kinetics of radical polymerization with an ultrafast coherent Raman microscope. Adv. Sci. (Weinh) *7*, 1903644.
44. Freudiger, C.W., Min, W., Saar, B.G., Lu, S., Holtom, G.R., He, C., Tsai, J.C., Kang, J.X., and Xie, X.S. (2008). Label-free biomedical imaging with high sensitivity by stimulated Raman scattering microscopy. Science *322*, 1857–1861.
45. Cheng, Q., Miao, Y., Wild, J., Min, W., and Yang, Y. (2021). Emerging applications of stimulated Raman scattering microscopy in materials science. Matter *4*, 1460–1483.
46. Bai, P., Li, J., Brushett, F.R., and Bazant, M.Z. (2016). Transition of lithium growth mechanisms in liquid electrolytes. Energy Environ. Sci. *9*, 3221–3229.
47. Alarco, P.-J., Abu-Lebdeh, Y., Abouimrane, A., and Armand, M. (2004). The plastic-crystalline phase of succinonitrile as a universal matrix for solid-state ionic conductors. Nat. Mater. *3*, 476–481.
48. Brouillette, D., Irish, D.E., Taylor, N.J., Perron, G., Odziemkowski, M., and Desnoyers, J.E. (2002). Stable solvates in solution of lithium bis (trifluoromethylsulfone) imide in glymes and other aprotic solvents: phase diagrams, crystallography and Raman spectroscopy. Phys. Chem. Chem. Phys. *4*, 6063–6071.
49. Fengler, O.I., and Ruoff, A. (2001). Vibrational spectra of succinonitrile and its [1, 4-$^{13}C_2$]-,[2, 2, 3, 3-$^2H_4$]-and [1,4-$^{13}C_2$-2, 2, 3, 3-$^2H_4$]-isotopomers and a force field of succinonitrile. Spectrochim. Acta A Mol. Biomol. Spectrosc. *57*, 105–117.
50. Miyazawa, T., Fukushima, K., and Ideguchi, Y. (1962). Molecular vibrations and structure of high polymers. III. Polarized infrared spectra, normal vibrations, and helical conformation of polyethylene glycol. J. Chem. Phys. *37*, 2764–2776.

Please cite this article in press as: Cheng et al., Stabilizing lithium plating in polymer electrolytes by concentration-polarization-induced phase transformation, Joule (2022), https://doi.org/10.1016/j.joule.2022.08.001

51. Yang, G., Sacci, R.L., Ivanov, I.N., Ruther, R.E., Hays, K.A., Zhang, Y., Cao, P.-F., Veith, G.M., Dudney, N.J., Saito, T., et al. (2019). Probing electrolyte solvents at solid/liquid interface using gap-mode surface-enhanced Raman spectroscopy. J. Electrochem. Soc. *166*, A178–A187.

52. Marzantowicz, M., Dygas, J.R., Krok, F., Tomaszewska, A., Żukowska, G.Z., Florjańczyk, Z., and Zygadło-Monikowska, E. (2010). Phase segregation phenomena in poly (ethylene oxide): LiN $(CF_3SO_2)_2$ electrolyte studied by local Raman spectroscopy. Electrochim. Acta *55*, 5446–5452.

53. Sneddon, I.N. (1948). Boussinesq's problem for a rigid cone. Math. Proc. Camb. Phil. Soc. *44*, 492–507.

54. Fincher, C.D., Ojeda, D., Zhang, Y., Pharr, G.M., and Pharr, M. (2020). Mechanical properties of metallic lithium: from nano to bulk scales. Acta Mater. *186*, 215–222.

55. Bellan, L.M., Kameoka, J., and Craighead, H.G. (2005). Measurement of the Young's moduli of individual polyethylene oxide and glass nanofibres. Nanotechnology *16*, 1095–1099.

56. Nie, H.-Y., Motomatsu, M., Mizutani, W., and Tokumoto, H. (1995). Local modification of elastic properties of polystyrene–polyethyleneoxide blend surfaces. J. Vac. Sci. Technol. B *13*, 1163–1166.

57. Brissot, C., Rosso, M., Chazalviel, J.-N., and Lascaud, S. (1999). Dendritic growth mechanisms in lithium/polymer cells. J. Power Sources *81–82*, 925–929.

58. Chazalviel, J.-N. (1990). Electrochemical aspects of the generation of ramified metallic electrodeposits. Phys. Rev. A *42*, 7355–7367.

59. Yang, G., Lehmann, M.L., Zhao, S., Li, B., Ge, S., Cao, P.-F., Delnick, F.M., Sokolov, A.P., Saito, T., and Nanda, J. (2021). Anomalously high elastic modulus of a poly (ethylene oxide)-based composite electrolyte. Energy Storage Mater. *35*, 431–442.

60. Yu, B., Duan, J., Cong, H., Xie, W., Liu, R., Zhuang, X., Wang, H., Qi, B., Xu, M., Wang, Z.L., and Zhou, J. (2020). Thermosensitive crystallization-boosted liquid thermocells for low-grade heat harvesting. Science *370*, 342–346.